ISPRS Journal of Photogrammetry and Remote Sensing 184 (2022) 19–30

Contents lists available at ScienceDirect

ISPRS Journal of Photogrammetry and Remote Sensing

journal homepage: www.elsevier.com/locate/isprsjprs

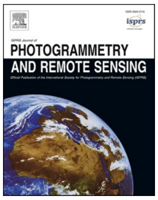

Mapping global flying aircraft activities using Landsat 8 and cloud computing

Fen Zhao [a,1], Lang Xia [a,1], Arve Kylling [b], Hua Shang [c], Peng Yang [a,*]

[a] Key Laboratory of Agricultural Remote Sensing (AGRIRS), Ministry of Agriculture and Rural Affairs Institute of Agricultural Resources and Regional Planning, Chinese Academy of Agricultural Sciences, Beijing 100081, China
[b] NILU-Norwegian Institute for Air Research, Kjeller, Norway
[c] Department of Ecology, Evolution and Natural Resources, Rutgers University, New Brunswick, NJ 08901, USA

ARTICLE INFO

Keywords:
Flying aircraft detection
Landsat 8
1.38 μm
Cloud computing
Global aviation
COVID-19

ABSTRACT

Satellite-based remote sensing might provide a potential way for monitoring the global flight activities and their environment impacts, while the remote sensing community pays less attention on it. In this study, we presented a flying aircraft detection algorithm which effectively handles the noise on Landsat 8 OLI cirrus band caused by energetic particles in the South Atlantic Anomaly region, and a new framework based on cloud infrastructure was proposed to map global flying aircraft activities from 2013 to 2020 using Landsat 8 Operational Land Imager (OLI) data. Validation was performed for 254 scenes recorded for various cloudy and surface conditions and vapor contents. The overall percentages of false alarms and omissions for these validation images were 5.37% and 7.80%, respectively. Limited to the resolution of Landsat data, cloud, the size and flight altitude of the aircraft, 42.99% flying aircraft were undetected compared with the FlightRadar24. Instead of using the Google Earth Engine, we employed more flexible cloud computing techniques, Google Cloud Storage and Google Calculation Engine, to construct our framework for the larger volume data. A total of 1.94 million Landsat images were analyzed to obtain the activities maps, and the results showed that globally flying aircraft increased by 25.85% from 2014 to 2019 (the year 2013 was excluded for the low coverage of Landsat scenes), with an annual rate of 4.31%. In 2020, flying aircraft were reduced by 40% compared with 2019 due to the influence of COVID-19 and traveling restrictions, and Europe was the most severely affected by COVID-19, with an 84.59% decline of flying aircraft in April 2020. This study provides a unique long-term supplement to monitor aviation activities and their climate impact.

1. Introduction

Over the past decades (1960–2018), aviation, as the fastest and most efficient way for long-distance travel, has continued to grow, with revenue passenger kilometers (RPK) increasing from 109 to 8269 billion km/yr (Lee et al., 2021). Aviation emissions, e.g., carbon dioxide (CO_2), nitrogen oxides (NO_x), and contrail cirrus, present strong net (warming) effective radiative forcing (ERF), thus raising concern about the supervision of flight activity and climate change impacts (Burkhardt and Kärcher, 2011; Sausen et al., 2005; Le et al., 2020; Skowron et al., 2021). Several studies have been conducted to understand and evaluate the impact of aviation on the climate system, but obtaining accurate results is still challenging (Penner, 1999; Kärcher et al., 2018; Skowron et al., 2021; Lee et al., 2021). One of the main reasons is the lack of direct observation data of flight activity spatially and temporally. Hence, the simulation process in the evaluation models had to be simplified, which introduced an uncertainty in the simulation results (Minnis et al., 1999; Schumann 2012; Chen and Gettelman, 2013; Bock and Burkhardt, 2016; Kärcher et al., 2018). Moreover, an evaluation of the aviation industry rebound after the influence of COVID-19 or making reasonable policies to further reduce emissions also require accurate and timely information of flight activity, which remain scattered and intermittent (Schumann et al., 2021).

The most common ways to trace the activity of flying aircraft are ground radar and automatic dependent surveillance broadcast (ADS-B) receivers (Costin and Francillon, 2012). In theory, these two methods

---

* Corresponding author.
E-mail address: yangpeng@caas.cn (P. Yang).
[1] Contributed equally to this work.

https://doi.org/10.1016/j.isprsjprs.2021.12.003
Received 30 September 2021; Received in revised form 15 November 2021; Accepted 3 December 2021

may achieve the best accuracy for tracing aircraft, but have limited coverage on a global scale. Ground radar is usually placed at airports or at fixed positions to monitor specific regions. As a result, only 30% of flying aircraft can be tracked (Liu et al., 2020). The ADS-B receiver usually covers regions with frequent human activities, thus the coverage is generally poor for remote locations, such as oceans or desert regions. In addition, the small number of aircraft not equipped with an ADS-B device cannot be traced by an ADS-B receiver (Zhao et al., 2018).

Satellite remote sensing provides another opportunity to monitor the activity of flying aircraft. High-resolution satellite images (e.g., Ikonos and World View), combined with morphological characteristics, machine learning, or even deep learning technology can satisfactorily identify parked aircraft (Liu et al., 2013; Wu et al., 2015; Zhang and Zhang, 2017; Wei et al., 2020; Shi et al. 2021). Considering the very long repeat cycle and high expense, high-resolution satellite data are not a suitable data source for monitoring flying aircraft globally. Hence, it is often used to monitor parked aircraft at airports or military bases (Wu et al., 2020).

Moderate resolution satellite instruments with relatively high repeat cycles and suitable resolution present a potential opportunity to monitor the global activity of flying aircraft, but until recently, few algorithms have been proposed to identify flying aircraft. The first state-of-art flying aircraft detection method proposed by Zhao et al. (2018) demonstrated the capability to detect flying aircraft using the Landsat 8 Operational Land Imager (OLI) cirrus channel (band 9). The algorithm uses the cirrus band located in the strong vapor absorption region. Due to the relatively high altitude of flying aircraft, the vapor between the aircraft and satellite sensor is lower than that between the ground and the satellite sensor (Zhao et al., 2018). The signal from the ground will thus be greatly attenuated, while the signal from the flying aircraft will be less influenced. Further investigation found that the Landsat OLI cirrus band is heavily influenced by energetic particles from the space over the South American region, which brings in many false alarms. Another method detecting and measuring the speed of flying aircraft is to use the parallax effect caused by the push-room design of satellite sensors, as presented by Heiselberg et al (2019) and Liu et al (2020) for Sentinel 2 Multispectral Instrument (MSI). Methods based on the parallax effect mainly rely on the reflectance difference between the background and the fast-moving objects, which may be influenced by the high reflectance, e.g., cloudy scenes, snow-covered landscapes, deserts, and even man-made surfaces. But this problem can be relieved by jointing other MSI bands, e.g., short-wave near infrared or cirrus bands (Liu et al., 2020), or the velocity and position for the fast-moving objects (Heiselberg et al., 2021).

To trace and map the global activities of flying aircraft, an appropriate detection algorithm is the essential, and the technology to hand such large amounts of historical Landsat data efficiently and rapidly is another challenge. This study aims to construct an appropriate detection algorithm and a cloud framework for the larger volume of data to map the global activities of flying aircraft. First, we improved the algorithm of Zhao et al. (2018) for the South Atlantic Anomaly (SAA) region to eliminate false alarms caused by energetic particles on the OLI cirrus band, thus making our method applicable globally. Then, careful validation was performed to evaluate the performance of the algorithm. Finally, instead of using the Google Earth Engine (GEE), we used cloud computing, Google Cloud Store (GCS) and the Google Calculation Engine (GCE) to construct our framework for handling the global Landsat 8 OLI data. In all, 1.94 million Landsat 8 OLI images were analyzed relying on the proposed framework to map the global activities of flying aircraft from 2013 to 2020.

2. Algorithm and improvement

2.1. Algorithm

Sitting in the region of a strong vapor absorption band, the 1.38 μm channel is quite useful for observing objects at high altitude, such as cirrus clouds, volcanic ash and flying aircraft (Gao and Kaufman, 1995; Frey et al., 2008; Xia. et al., 2015; Xia et al., 2018). In our previous algorithm, aircraft detection was divided into two scenes: dry scene and cloudy scene that is also called “normal scene” in this article. The dry scene means that the vapor is low (less than 0.8 g/cm^2) and not large enough to mask the reflectance from the ground. The normal scene means that the vapor (greater than 0.8 g/cm^2) is large enough to mask the ground reflectance, and includes clear-sky and cloudy scene in this study.

According to the size of flying aircraft and the resolution of OLI cirrus band, flying aircraft in OLI cirrus band visibly are often composed of a small number of pixels, e.g., 2–12, similar to the outlier in the images. Hence, a composition of the Laplacian and Sobel operators, as presented in Zhao et al. (2018), is used to segment the potential aircraft. Eq. (1) is used to determine whether the segmentation result can be identified as a real aircraft in a normal scene:

$$Aircraft=\begin{cases} true, R_{asp}>0.45 and R_{pix}>0.6 and 6<N_{airc}<15 and DN_{MVPA}>Max(S) \\ false, otherwise \end{cases} \tag{1}$$

where R_{asp} is the aspect ratio of the segmented image, N_{airc} indicates the pixel number of a potential aircraft in the segmentation image, R_{pix} indicates the ratio of N_{airc} and the total pixel number of the segmentation image, $MVPA$ is the maximum value point among the potential aircraft pixels, DN_{MVPA} is the digital number (DN) value of the maximum value point among the potential aircraft pixels, S is a square with a width of 15 pixels and the center of $MVPA$, and $Max(S)$ is the maximum pixel value of S. $Aircraft$ is the result of aircraft detection.

The push-room designation of the OLI sensor makes the inter-band offsets for objects with a high moving speed. This implies that the flying aircraft in each band of OLI are presented at different row and column numbers, while ground objects share the same row and column numbers. The equation shown in Eq. (2) is used to further remove false alarms under a low vapor scene (dry scene).

$$Aircraft = \begin{cases} true, DN_{i,j} < AccPer_{0.95}(Hist(S_{2.1})) \\ false, otherwise \end{cases} \tag{2}$$

Here, i, j is the row and column numbers of $MVPA$, $DN_{i,j}$ is the image DN value of the 2.1 μm channel with a row and column of i, j, $S_{2.1}$ is a square with the center at i and j, and a width of 15 pixels, and $Hist(S_{2.1})$ is the histogram result of S. $AccPer_{0.95}(Hist(S_{2.1}))$ presents the DN value in which the accumulation percentage in $Hist(S_{2.1})$ is greater than 0.95.

2.2. Improvement of the SAA region

The SAA is a region where the inner Van Allen belt dips down to an altitude of 200 km and is closest to the Earth’s surface over the South Atlantic Ocean (Finlay et al., 2020). This phenomenon is caused by the tilted angle of approximately 11° between the Earth’s rotational axis of rotation and the Earth’s magnetic axis, which is the axis of symmetry for the Van Allen radiation belts. Due to the weak Earth magnetic field in the SAA region, orbiting satellites and their sensors are exposed to a high flux of energetic particles, thus leading to bright spots in the obtained images. Except for the southern Atlantic Ocean and part of South America, polar-orbiting satellites crossing the north and south poles may be influenced by energetic particles.

As shown in Fig. 1(A)–(H), OLI band 9 in the SAA region is heavily contaminated by energetic particles, and some bright spots formed from several pixels can be observed from the images. The noisy features share similar shapes and sizes with aircraft, as shown in Fig. 1(I)–(P), so these features can be easily misclassified as aircraft with the current algorithm. However, these noisy points usually appear in only one channel at the time; therefore, it is impossible to correct this problem using inter-band information.

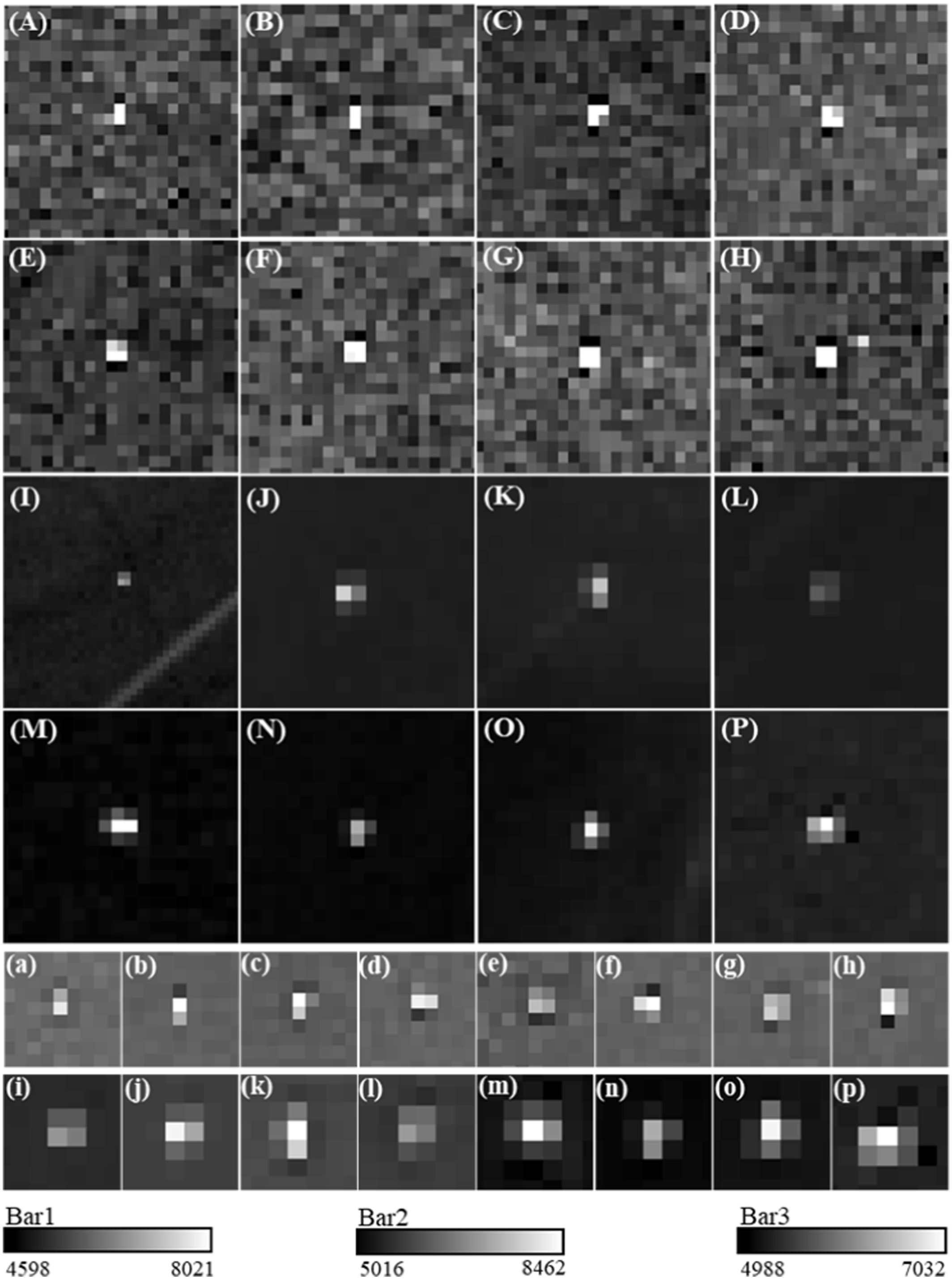

Fig. 1. Pixels of bright spots contaminated by energetic particles ((A)-(H)) and aircraft ((I)-(P)), and the corresponding magnified images ((a)-(p)). Notes: (A)-(H) are captured on October 2, 2019 with World Reference System (WRS) path/row of 221/73 over Minas Gerais, Brazil, (I)-(L) are captured on April 3, 2015 with path/row of 39/36 over Las Vegas, U.S., (M)-(P) are captured on May 25, 2017 with path/row of 121/36 over Linyi, China. (a)-(p) are the magnified images for (A)-(P), respectively. Bar1, Bar2, and Bar3 are grayscales for (A)-(H), (I)-(L) and (M)-(P).

After being hit by energetic particles, the affected detectors recoil in bright target recovery, and one or more surrounding dark pixels can usually be observed (Elamaran et al., 2018). Besides, as the dark pixels are the response of the bright pixels, the darkest pixel and the brightest pixel are often adjacent. Additionally, the brighter the bright pixels are, the blacker the black pixels. As shown in Fig. 1(A)–(D), the bright points are often surrounded by one or more dark pixels, regardless of the shape of the bright point. Fig. 1(a)–(h) and (i)–(p) are the enlargements of the noise pixels in Fig. 1(A)–(H) and aircraft in Fig. 1(I)–(P), respectively. A square root stretching method was used to enhance the visualization for (a)–(p), but a 2% linear stretching for (A)-(P). As seen from Fig. 1(a)–(h), the darkest pixel and the brightest pixel are almost 4-adjacency, while the 4-adjacency is less observed for the pixels of the aircraft (except for Fig. 1(p)). This feature is significantly different from the flying aircraft in the images, even though the shade of aircraft may be present as dark pixels in the images. In this study, we used this feature to further eliminate false alarms in the SAA region.

First, we used the equation below to segment the aircraft pixels from a square centered on *MVPA* with a width of 5 pixels:

$$Pixel_{air} = \begin{cases} DN_s > 1.05 \times Mean(S_{s5}) \\ false, otherwise \end{cases} \tag{3}$$

where S_{s5} is the square centered on *MVPA* with a width of 5 pixels, $Mean(S_{s5})$ is the mean DN value of S_{s5}, DN_s is the DN value of pixel within the S_{s5}, and $Pixel_{air}$ is the pixels forming the aircraft. The value of 1.05 is obtained by experiences repeatedly, to minimize the false alarms and omissions.

Then, dark pixels surrounding $Pixel_{air}$ can be obtained by Eq. (4).

$$Pixel_{dark} = \begin{cases} DN_{sr} < Mean(S) \\ false, otherwise \end{cases} \tag{4}$$

where DN_{sr} is the DN value of the pixel within S and surrounding $Pixel_{air}$, $Mean(S)$ is the mean DN value of S, and $Pixel_{dark}$ is the dark pixel surrounding $Pixel_{air}$.

The rule with two parts was used to eliminate false alarms caused by energetic particles. (I) if the darkest pixel among $Pixel_{dark}$ is one of the 4 adjacent brightest pixels, it belongs to the potential aircraft pixels. Besides, for the bright spots composed of a small number of pixels, as shown in Fig. 1 (a) and (b), we adopted (II) that the potential aircraft is identified as a noise point when the pixel number of $Pixel_{air}$ is less than 2. We call the method presented in this section the SAA method for aircraft identification.

Fig. 2 shows a scene over South America for which the Landsat 8 OLI image is heavily contaminated by energetic particles. This image obtained on October 2, 2019, with a path/row of 221/73 was used to detect flying aircraft with or without the SAA method, and the detection results display significant differences (Fig. 2(c) and (d), respectively). The lines presented in Fig. 2(b) are the flight paths from FlightRadar24 during the Landsat imaging time. The red and yellow lines indicate that no flying aircraft signal on OLI band 9 is observed along the flight paths because of the low cruise altitude (less than3500 m) or small size of the aircraft. The orange lines present the detected flying aircraft along the flight paths, and thus, the two aircraft tracking methods achieve the

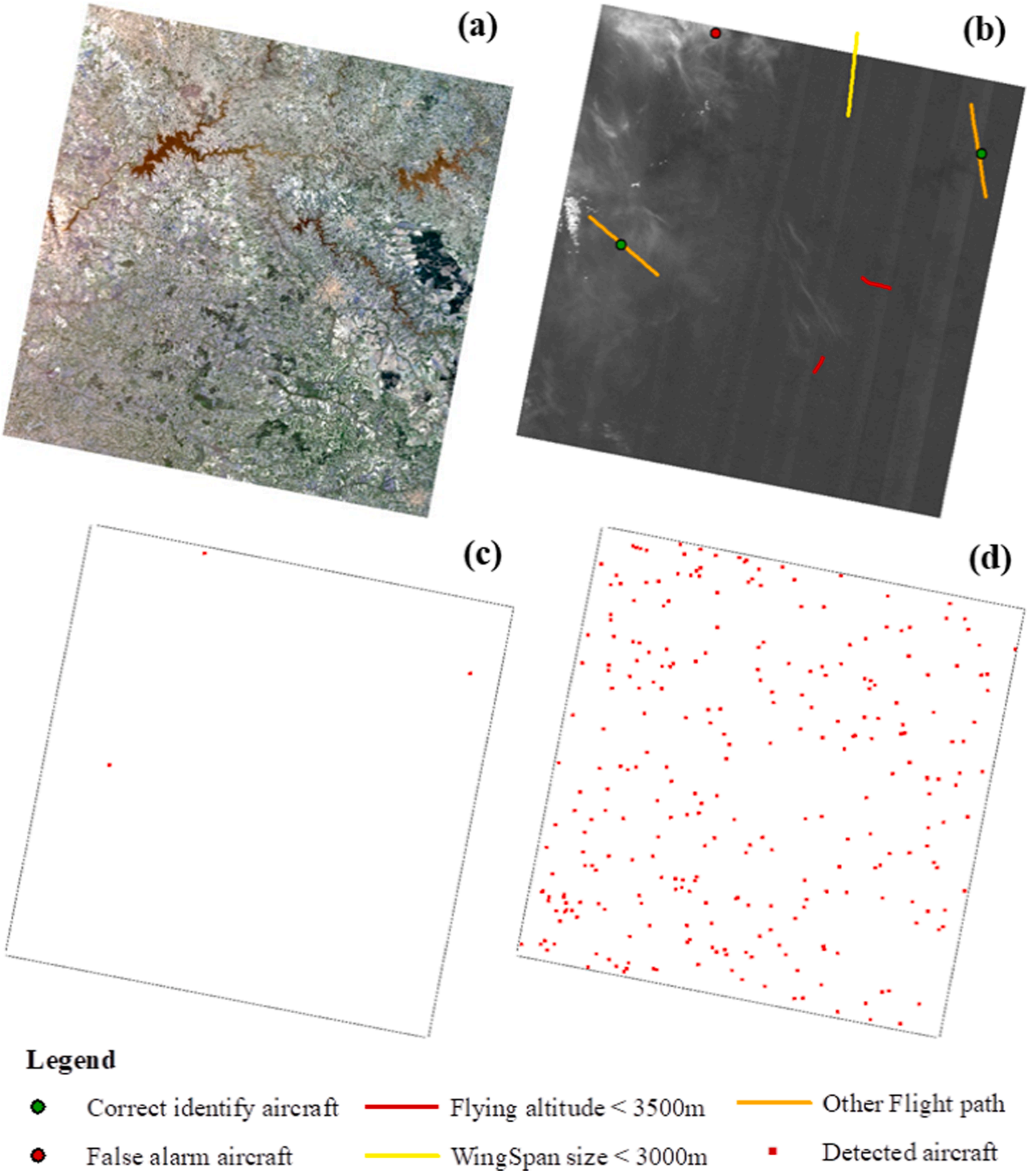

Fig. 2. Image and detection results of flying aircraft in the SAA region: (a) true color image of Landsat OLI data, (b) the image of OLI band 9 with flight paths overlaying, (c) the result with the SAA method, and (d) the result without using the SAA method.

same results (Fig. 2(b) and (c)). The red points shown in Fig. 2(c) and (d) are the detected flying aircraft from OLI data.

As is evident from Fig. 2, the SAA method just falsely identifies one aircraft, the red point at the top left of Fig. 2(b) and (c), while without using the SAA method, a large number of false alarms appear (Fig. 2(d)). Overall, the SAA method eliminates most of the influence of energetic particles, and a more reasonable result is obtained.

2.3. Data and framework

In this study, the detection algorithm was applied for Landsat 8 Collection 1 Level-1 data (Irons et al., 2012). Landsat 8 is the eighth satellite in the Landsat program, which was launched on Feb. 11, 2013 and carries OLI and thermal infrared sensor (TIRS) instruments to provide global coverage every 16 days. The OLI observes the Earth at two resolutions, 15 m for the panchromatic band and 30 m for the multispectral bands, with a swath width of 185 km. A total of 1.94 million OLI images from April 1, 2013 to December 31, 2020 were selected to map the activities of global flying aircraft.

The hourly vapor content data (total_column_water_vapor) from the European Centre for Medium-Range Weather Forecasts (ECMWF) Reanalysis 5th (ERA5) were used to provide detailed water vapor information. ERA5 is the fifth generation of the ECMWF atmospheric reanalysis of the global climate, which replaced ERA-Interim to provide a highly accurate numerical description of the recent climate (Hersbach et al., 2020). The ERA5 vapor data include the atmospheric total vapor content hourly, with a spatial resolution of 0.125°. In addition, real-time flying aircraft tracking data from FlightRadar24 (https://www.flightradar24.com/) were selected as a data source for validation.

Cloud computing provides the possibility for private individuals or institutions to perform tasks that require large-scale and high-performance computing with low cost and short waiting time. For example, the GEE based on the Google cloud computing infrastructure provides the planetary-scale computing service for all kinds of users (Gorelick et al., 2017; Murray et al., 2019; Tamiminia et al., 2020). Although the GEE is a powerful facility for remote sensing applications, it is unsuitable for identifying flying aircraft. The GEE hides every aspect of how a computation is managed, which means that applications that do not match the Earth Engine's computational model cannot be performed effectively (Gorelick et al., 2017). Instead of using the GEE directly, we use GCS and GCE from the Google Cloud Platform to construct a scalable framework to meet the requirement of handling massive OLI data on a global scale.

The framework for mapping activities of global flying aircraft deployed on the Google Cloud Platform is displayed in Fig. 3. Landsat data and water vapor content data were obtained from GCS and Copernicus Climate Data Store using Google Big Query and the ERA5 CDS API, respectively. Then, aircraft were detected on the GCS by multi-virtual machines handling the large size of volume data and satisfying the requirements of tremendous computing resources. In the process, the

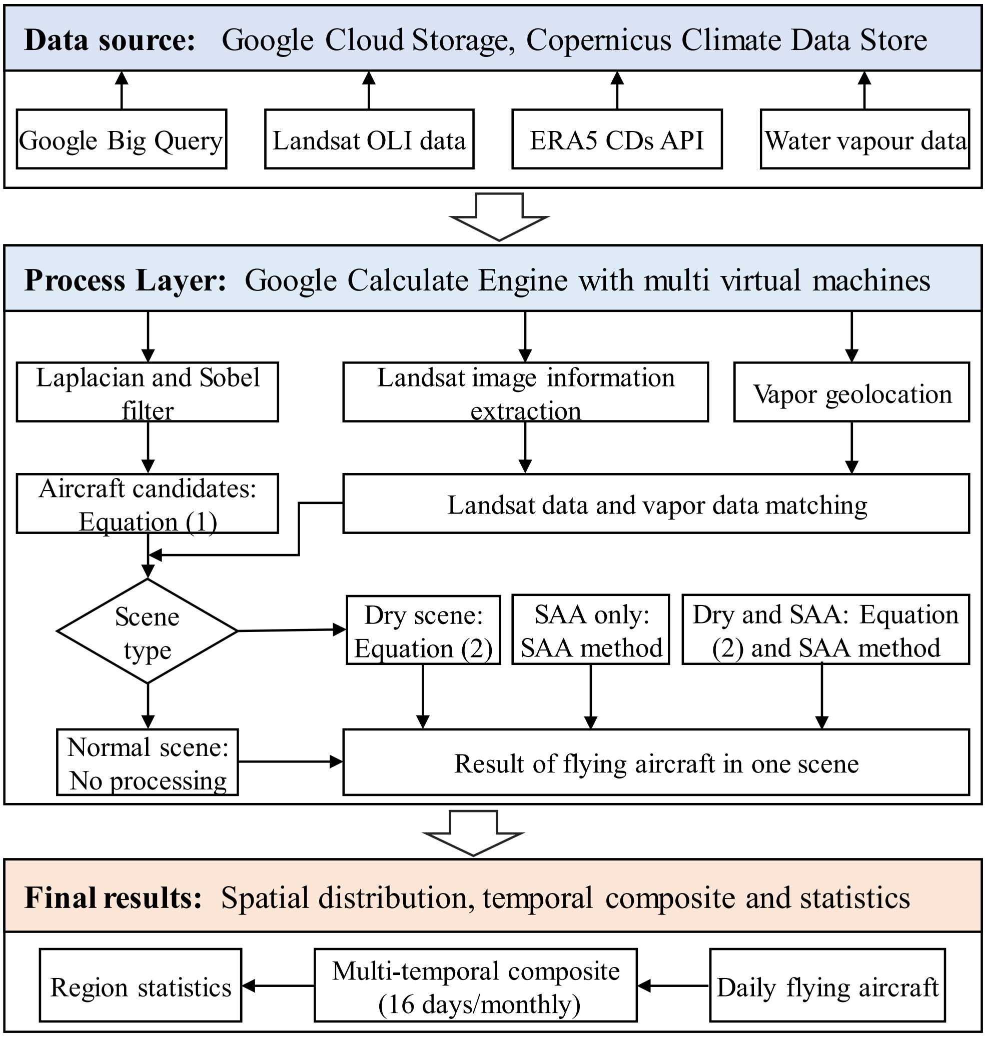

Fig. 3. Workflow of generating global flying aircraft data.

aircraft candidates and water vapor data were processed first. Then, according to the water vapor content and the region, the processing was classified into one of four types: normal scene, dry scene, SAA, and both SAA and dry scene. Finally, the aircraft were identified using the method presented in the study. Once all the daily data were generated, multitemporal composites were made to obtain different maps of flight activities, e.g., a 16-day composition to obtain the global coverage.

In this study, the SAA method was applied to the SAA region and used for the North Pole where the latitude was larger than 65°. According to the region of SAA presented by Liu et al. (2018) and Finlay et al. (2020), and the false alarm distribution of detected flying aircraft in practice, the paths/rows 0–47/58–104 and 157–233/58–104 of Landsat scenes were selected as the SAA region. For the Tibetan region, very few aircraft pass through this region due to the high altitude, thus we removed this region to reduce the computing burden. For the same reason, the Landsat images covering the Antarctic region have also been removed.

3. Validation

Landsat 8 images over the regions of China, America, Europe, Africa, Australia, and South America were selected for validation, and the results are summarized in Table 1. For China, America, Europe, and Africa, Landsat 8 images from December 1, 2017 to January 01, 2018 were used, and Landsat images from August 1, 2019 to October 31, 2019 were adopted for Australia and South America. These images include a variety of background surfaces, e.g., snow, desert, urban, forest, grass, mountains, and different cloud coverages, under different water vapor contents. More specifically, most of the images were obtained when the water vapor content was quite low (less than 0.8 g/cm^2) for China and America. For the European and Australian regions, most images are cloud contaminated, while the cloud coverage over the Chinese and African regions is quite low.

In this study, except for the African region, the other validation regions are all well covered by the ground aircraft tracker to ensure the real-time aircraft tracking data available from FlightRadar24. For Landsat 8 OLI images obtained in these regions, if no available real-time monitoring data are available from FlightRadar24, these scenes are removed from the validation (not applying to the African region). Finally, 254 Landsat 8 OLI images were used for validation.

The actual distribution of flying aircraft for algorithm validation was obtained by manual interpretation. The manual interpretation was carefully performed based on the parallax effect displayed in the OLI images, and the real-time aircraft tracking data were obtained from FlightRadar24. Here, the Landsat band 4, 3, 2 were selected to compose true-color image, and the displacement of flying aircraft in the images due to the parallax effect was used as the reference for manual interpretation. The aircraft covered by clouds, with lengths less than the resolution of Landsat images, and at low flying altitudes, found in the real-time data from FlightRadar24 but not in the OLI band 9 images were removed from the manual interpretation results.

Notes: 'Image Num.' is the number of OLI images used for validation. 'Study Num.' presents the aircraft numbers identified by the study, 'Manual Num.' presents the aircraft numbers identified by the manual interpretation. 'Accuracy/False' means the number of other objects falsely recognized as aircraft by the algorithm, and 'Accuracy/Omission' indicates the number of aircraft that failed to be identified by the algorithm; nevertheless, it is confirmed by manual interpretation. 'Accuracy/False' and 'Accuracy/Omission' refer to the ratio of false alarms and omissions to total numbers of the algorithm, respectively. The detailed result of each scene can be found in the supplement materials Table 1.

For the South American region, the ratio of false alarms was 6.03%, similar to other regions, such as 5.85% for the Chinese region and 6.77% for the American region. The low false alarm ratio indicates that the SAA method can successfully eliminate the influences of energetic particles. On the other hand, the omission ratio of 23.28% is larger than other regions, e.g., 10.98% for the Australian region and 4.59% for the American region. The omission ratio of the South American region was even significantly larger than that of the European region (12.52%), where images were heavily covered by clouds. To clarify how the SAA method affects the number of omissions, we also performed detection without the SAA method on the images of the South American region. The results showed that using the SAA method increased the omission number of aircraft from 5 to 27 and led to approximately 18.97% (22/116) omission in the South American region accordingly. Further analysis indicated that the rule part (I) presented in section 2.2 led to approximately 45% (10/22) omissions, while rule part (II) contributed the additional part.

For Europe and Australia, the omission ratios are obviously larger than those in the other regions due to the high coverage of high clouds, with values of 12.52% and 10.98%, respectively. High clouds give high reflectance in OLI band 9, which makes the edge between the background and aircraft indistinguishable, and the segmentation algorithm fails to process these scenes correctly. For dry scenes, such as Chinese and American regions, the ratios of omissions and false alarms were all lower than those in the other regions. In general, a total of 1807 flying aircraft were recognized from 254 Landsat 8 images, and the percentages of false alarms and omissions for the validation data were 5.37% and 7.80%, respectively.

Furthermore, we analyzed the difference in detected flying aircraft between this study and the real-time data from FlightRadar24. The flying aircraft not presented in OLI band 9, caused by low flying altitude (less than 3500 m), small size (wingspan less than 30 m), or covered by clouds (cannot be observed on band 9 clearly), are summarized for each region, as the column 'Omission of this study' shown in Table 2. The flying aircraft failed to be traced by FlightRadar24, but the aircraft detected in this study are also presented in the table.

In general, a total of 2842 aircraft were detected by FlightRadar24, thus 42.99% (1222/2842) were undetected by the study. Among the undetected flying aircraft, 40.59% (496/1222) were due to the low flying altitude (less than 3500 m), 19.63% (240/1222) were due to the small size of the aircraft, and 45.90% (561/1222) were caused by cloud contamination. Note that omissions caused by flying altitude or size may be counted repeatedly (no more than 75) for aircraft with a small size usually flying at a low altitude. The omission caused by a low flying

Table 1
Results of accuracy validation for the algorithm.

Region	Path/Row	Image Num.	Study Num.	Manual Num.	Accuracy (%)		Accuracy (%)	
					False	Omission	False	Omission
America	27–29/33–36	34	458	448	31	21	6.77	4.59
Europe	196–198/24–27	40	567	619	19	71	3.35	12.52
China	123–124/34–40	45	564	543	33	12	5.85	2.13
Australia	92–94/83–85	40	82	86	5	9	6.10	10.98
Africa	179–181/49–51	44	20	19	2	1	10.00	5.00
South America	219–220/72–77	51	116	136	7	27	6.03	23.28
Total		254	1807	1851	97	141	5.37	7.80

Table 2
Comparison of detected aircraft results between this study and FlightRadar24.

Region	Total aircraft Num.		Omission of this study				Omission of FlightRadar24
	Study	FlightRadar24	Altitude	Size	Cloud	Total	
America	458	692	121	40	82	227	17
Europe	567	1216	266	128	456	811	10
China	564	554	8	11	8	25	24
Australia	82	124	34	5	7	44	3
Africa	20	/	/	/	/	/	18
South America	116	256	67	56	8	115	18
Total	1807	2842	496	240	560	1222	90

Notes: ‘Altitude’, ‘Size’ and ‘Cloud’ stand for the situation caused by low flying altitude, small size, and covered by clouds, respectively. ‘/’ means data is not available.

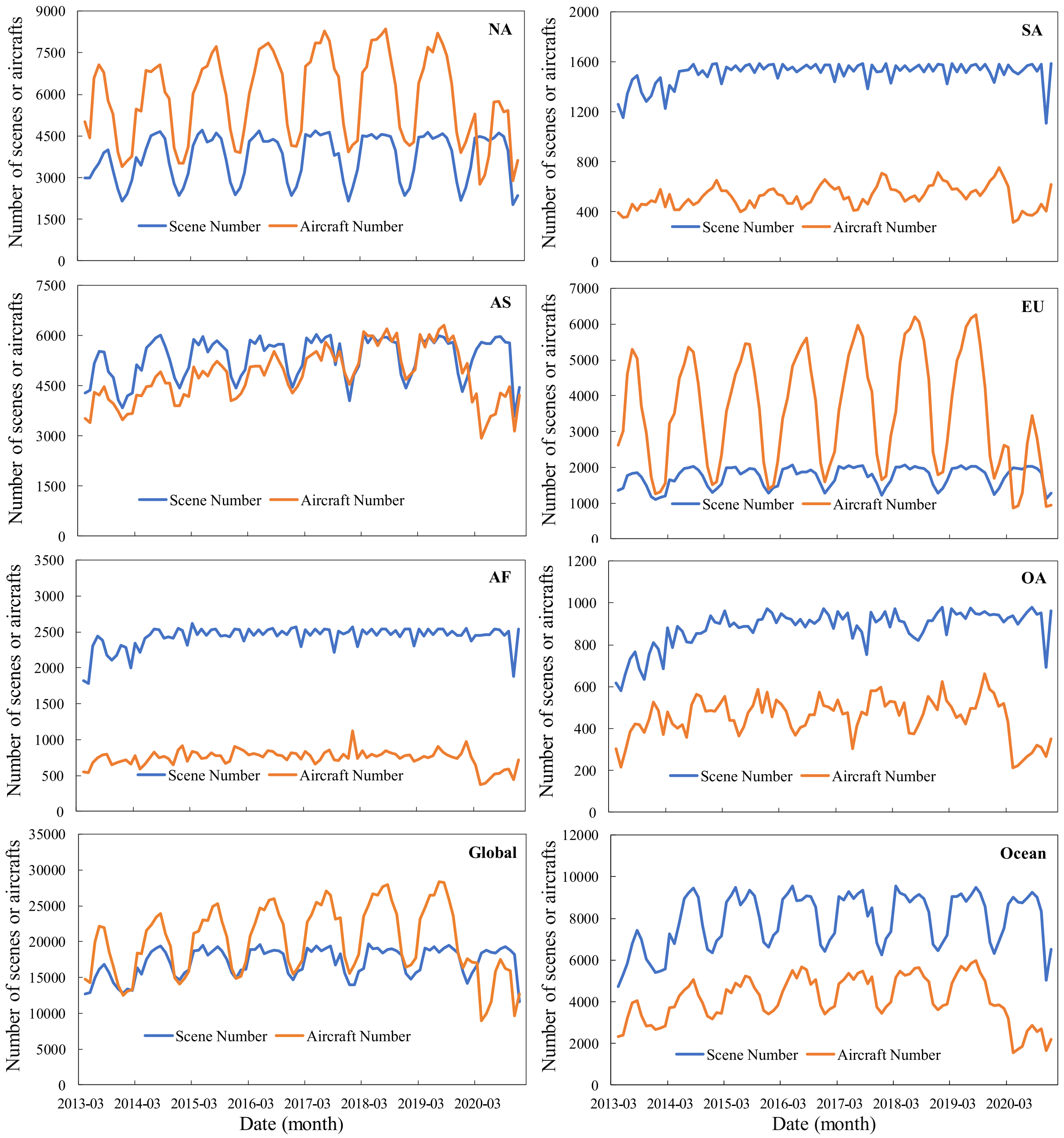

Fig. 4. The number of flying aircraft detected for Global North America, Africa, Asia, Europe, South America, Oceania, and other regions. Notes: NA = North America, SA = North America, EU = Europe, OA = Oceania, AF = Africa, AS = Asia. Ocean refers to the regions other than these above continents.

altitude was generally found near the airport during take-off and landing. The validation images for Europe, America and South America contain more airports than other regions; as a result, the omission due to a low flying altitude was larger than that in the other regions. For example, the omission and total number of detected aircraft in Europe were 266 and 567, but were 8 and 564 in China regions respectively. The omission caused by clouds can be found anytime, not only during take-off and landing but also during cruising, once the altitude of the cloud and optical thickness are enough to mask the signal of flying aircraft.

Compared with the results presented in this study, a total of 90 flying aircraft were undetected by FlightRadar24. This omission of FlightRadar24 is due to two main reasons. One is attributed to the coverage gaps of ADS-B receivers, e.g., as in the African region shown in Table 2. Another reason is that some aircraft are not equipped with ADS-B transponders. Overall, this study provides a supplement for monitoring the activities of aviation, especially for regions without enough or stable coverage of ADS-B devices.

4. Results and application

After processing 1.94 million Landsat OLI images on the Google Cloud Platform, we obtained the spatial–temporal map of global flying aircraft from April 1, 2013 to December 31, 2020, and 1.87 million aircraft were identified in total. The numbers of global flying aircraft identified from Landsat 8 OLI images monthly during the last few years are presented in Fig. 4. From 2013 to 2019, the number of global flying aircraft shows a significantly increasing trend, both in summer and winter. In general, flying aircraft rose by 25.85% from 2014 to 2019 with an annual growth rate of 4.31%, close to that of the air traffic data predicted by Airbus (2014), with 4.4% annual growth from 2013 to 2033. One thing to note here, the year 2013 is excluded from the calculation, for the low coverage of Landsat data in 2013 on global scale. In 2020, the total flying aircraft decreased by 40% compared with 2019 due to the influence of COVID-19. For reference, the decline of RPK in 2020 released by the International Civil Aviation Organization (ICAO)

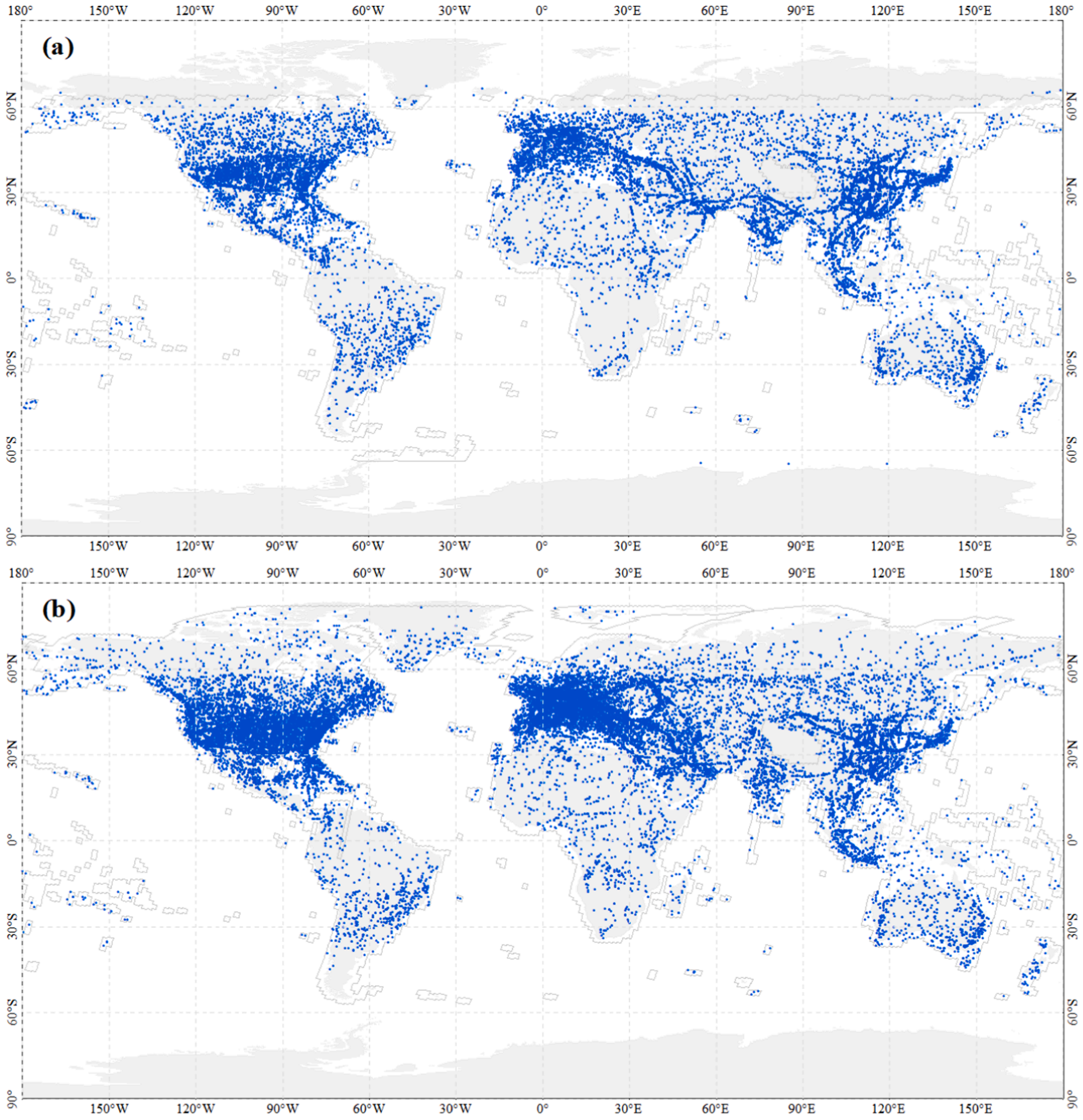

Fig. 5. Flying aircraft detected in (a) January 2019 and (b) July 2019 from Landsat OLI images. Notes: The gray line is the coverage of Landsat images, and the gray area represents the land.

(ICAO, 2020) is 53% of that in 2019. Among continents, Asia is the fastest growing continent in aviation, while Oceania, Africa, and South America present slower growth.

In the Northern Hemisphere, the total flying aircraft number in summer is 68.37% greater than that in winter for two reasons. The first is the coverage of the Landsat image. The less coverage there is, the fewer detected flying aircraft there are. The total numbers of Landsat 8 OLI images monthly from April 1, 2013 to December 31, 2020 are presented in Fig. 4, showing that the number of Landsat images is 30% lower in winter than in summer. In addition, another important reason is that the travel demand is higher in summer than in winter; as a result, aviation activities are much more frequent in summer than in winter. Therefore, fewer flying aircraft are detected in winter.

The spatial distribution of flying aircraft is presented in Fig. 5. The flying aircraft detected by Landsat 8 data in January and July 2019 were selected to display the activities of aircraft globally. As shown in Fig. 5, aircraft are mainly distributed over the Northern Hemisphere and cluster together in North America, Europe and East Asia, roughly totaling 70.82% of all aircraft worldwide. The density of aircraft is closely related to regional economic development. The better the economy is, the greater the number of aircraft. Additionally, almost no aircraft are found at high latitudes (latitude > 65°) due to unavailable coverage of Landsat images in winter (Fig. 5(a)).

The COVID-19 pandemic outbreak has had an unmatched negative impact on the travel tourism industry worldwide, thus global aviation is hit accordingly. Here, our results present a view of how global aviation is influenced by COVID-19. The activity maps of flying aircraft within April 7 to 22, 2019 and April 6 to 21, 2020 are shown in Fig. 6(a) and (b), respectively. Compared with the period of April 7 to 22, 2019, the number of aircraft during April 6, 2020 to April 21, 2020 was reduced by 55.54%. Europe and America suffered the heaviest decrease in aviation activities, with declines of 84.59% and 58.55%, respectively, while Asia presented a smaller decrease in flying activities. The results conducted in this study illustrate the inhibitory effects of COVID-19 on global aviation

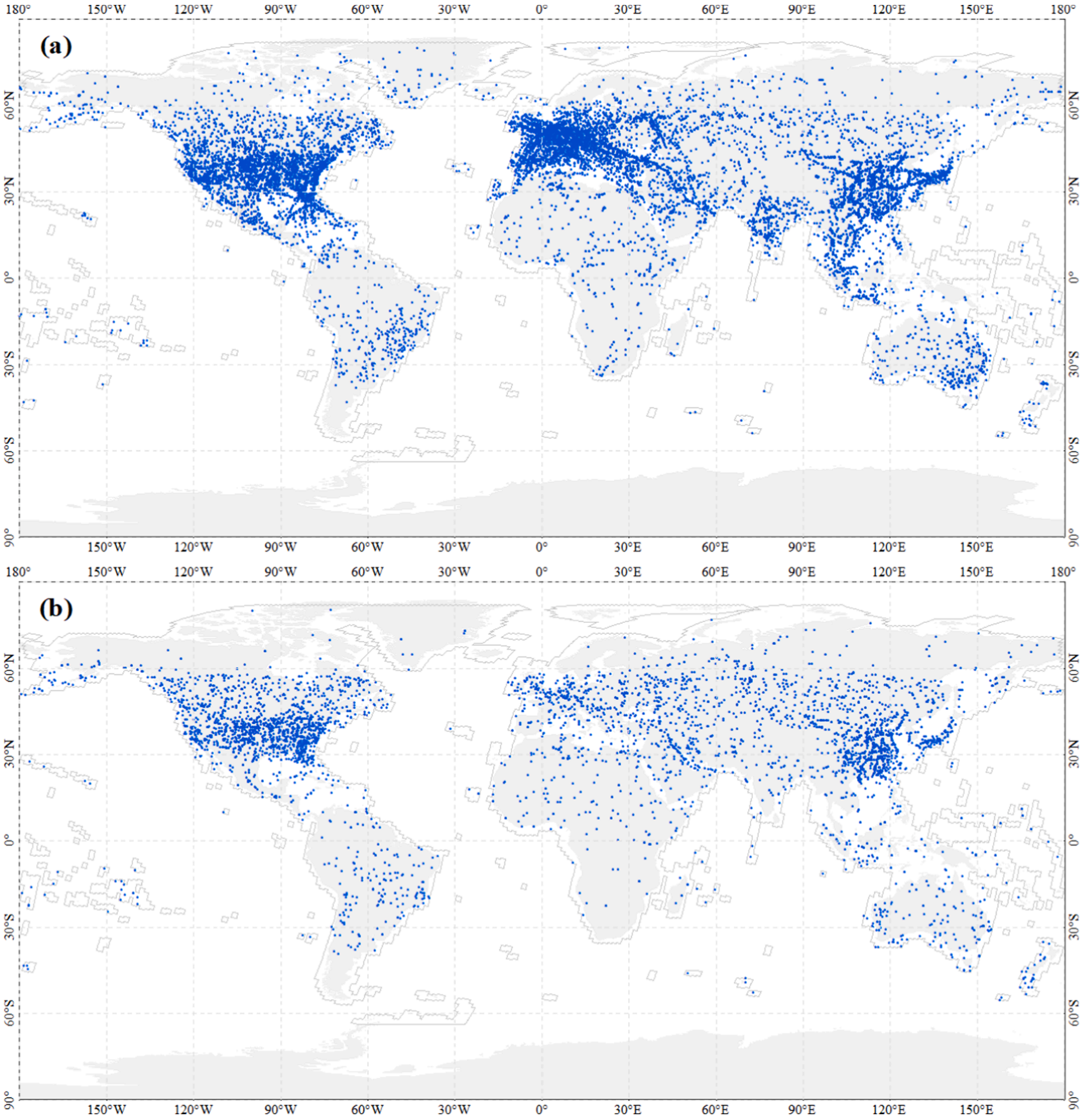

Fig. 6. Flying aircraft detected within (a) April 7 to 22, 2019 and (b) April 6 to 21, 2020 from Landsat OLI images. Notes: The gray line is the coverage of Landsat images, and the gray area represents the land.

well, which reflects that the detection algorithm of flying aircraft is authentic and valid.

Reduction rate of Aircraft number in 2020 compared to 2019 is presented in Fig. 7 to illustrate the impact of COVID-19 with time. In general, the number of global flying aircraft in 2020 is clearly lower than that in 2019. The number of global flying aircraft began to decline approximately March 2020 and dropped by 70% until April 2020, and then a slow recovery was observed. Among different continents, Europe is the most severely affected by COVID-19, with an 84.59% decline of flying aircraft in April 2020. Aviation in Asia was the first to respond to COVID-19, and the number of flights showed a significant decline in early February 2020. In terms of recovery, flights across the oceans, as shown in the other regions of Fig. 7, did not fully resume due to restrictions on international travel. Essentially, the changes in aviation activities in this study are consistent with the development trends of COVID-19, which suggests that the detection algorithm for flying aircraft can accurately capture the status of the aviation industry.

5. Discussion

The ground ADS-B device and the method presented in this study provide two different ways to map the flight activities. The ground ADS-B device demonstrates unique high accuracy to track the activities of aircraft. However, the main problems of this method are the coverage gap and stability of the ADS-B device, which are difficult to mitigate in remote locations. Until now, the coverage of ADS-B devices has been quite poor in North Africa, Northern Canada, Western China, Southern Venezuela, Northern Russian, and especially Siberia. The historical archive of flight activities is highly crucial for climate change research, but such information is not available from the newly deployed ADS-B devices. Before 2017, the coverage of ADS-B devices was mainly over in Europe, America and some large cities in other countries. This means that no flying aircraft information can be provided for most locales, but this study provides relatively long historical archive of flight activities, e.g., beginning 2013. However, this study also has some limitations and uncertainties.

The first limitation of the study is temporal coverage. The Landsat 8 satellite revisits the Earth with a cycle of 16 days, as a result, this study can only provide full cover every 16 days. In addition, the Landsat satellite sensor only records an instantaneous state of the object, while the ground ADS-B device can provide continuous observations of the aircraft during flight. More specifically, the Landsat 8 satellite overpasses and acquires images at approximately 10:30 AM local time, thus no flight information can be obtained at other times. The 10:30 AM local time is one of the busiest flight times during the day, which means that the map of flying aircraft presented in this study is likely the densest throughout the day. However, the launch of Landsat 9 at the end of 2021 could enhance the observation frequency (Masek et al., 2020).

The omission of flying aircraft with low flying altitudes or small sizes is the second limitation of our algorithm, which is mainly caused by the spatial resolution of Landsat data and vapor absorption at 1.38 μm. As shown in Table 2, approximately 37.30% (674/1807) of aircraft are omitted by the study compared to the real-time data from FlightRadar24 due to small size or low flying altitude. In addition, some uncertainties come from the vapor content data. We used water vapor data with a resolution of 0.125° in the study, which is currently the highest spatial resolution water vapor data available with high temporal resolution. Lower-resolution water vapor data increase the uncertainty of scene type determination. For example, if a day scene is falsely classified into a normal scene, Eq. (2) will not be used to eliminate potential false alarms. The method to eliminate potential false alarms in the SAA region also introduces the uncertainty of the detected results in the SAA region. As we discussed in section 3, the application of the SAA method increases the additional ratio of omission by 18.97%.

Another uncertainty is cloud coverage, which may occur anywhere and anytime and changes with the seasons. On the one hand, when the altitude of the cloud is high or the flight altitude of aircraft is low, and the optical thickness of the cloud is enough to mask the signal of the flying aircraft, all the aircraft will be omitted by the detected algorithm. On the other hand, although the optical thickness of the cloud is not enough to mask the signal of the flying aircraft, the cloud may weaken the difference between the cloud and aircraft, which invalidates the segmentation algorithm. As a result, the omission in cloud-affected scenes increases. However, the 1.38 μm band is less sensitive to low clouds or middle clouds, which means that this band is less influenced by clouds than the parallax method.

In this study, we used the Google Cloud (other cloud services are also appropriate, e.g., Amazon Web Services), GCS and GCE in place of the GEE to construct another solution with enough scalability. The service of GCS and GCE provides autoscaling capabilities for the user, therefore, the two core operations, Landsat data download from GCS and flying aircraft identification by GCE virtual machine, are also scalable. This means that the total processing time almost linearly decreases with the number of virtual machines. We used 10 virtual machines from GCE, and then all the Landsat 8 data were processed within 2 weeks, which indicates that the structures based on GCS and GCE are sufficiently scalable and flexible. This means that applications that do not match the GEE computational model, e.g., some machine learning models and operations that involve long-running iterative processes, can run efficiently under the GCS and GCE frameworks.

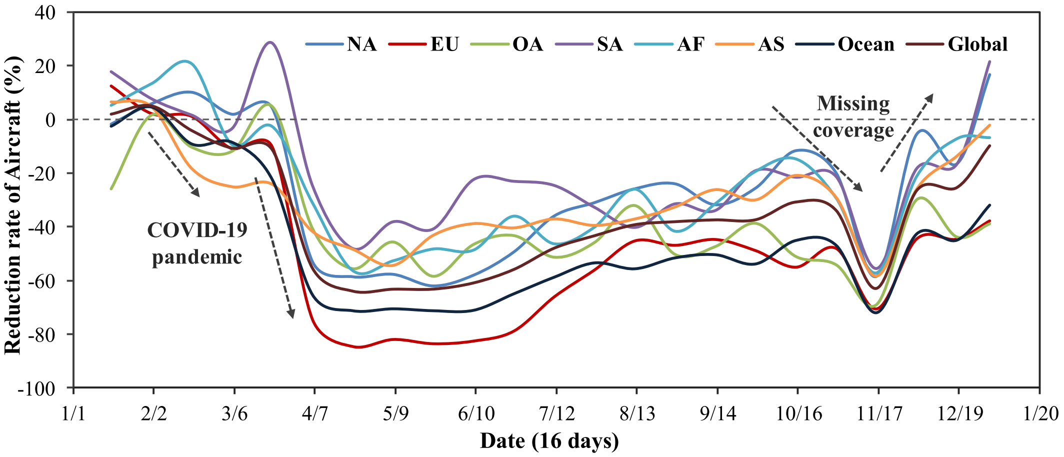

Fig. 7. Reduction rate of flying aircraft number in 2020 compared to 2019 detected by Landsat 8 OLI images every 16 days.

6. Conclusions

In this study, based on Landsat 8 OLI data and cloud computing, the first global activities maps of flying aircraft from April 1, 2013 to December 31, 2020 were presented. The described method reduces the influence of energetic particles in the South Atlantic Ocean. This was validated by an effective decrease in false positives for the South Atlantic Ocean. The validation over the 254 scenes for 6 regions suggested that the algorithm performs well, with false alarm and omission ratios of 5.37% and 7.80%, respectively. Furthermore, the computing framework constructed in this study to handle the large data volume relied on GCS and GCE, which proved to be both flexible and scalable. This framework is very useful for applications that require processing extremely large datasets but cannot share the benefits of distributed processing from the GEE.

The result of flying aircraft showed that flying aircraft from 2014 to 2019 increased by 25.85% with an annual rise of 4.31% on a global scale, while the total flying aircraft decreased by 40% in 2020 compared with 2019 due to the influence of COVID-19. We hope the result of this study will serve as the direct observation supplement for understanding and evaluating aviation's impacts on the climate system and aviation industry rebound after the influence of COVID-19.

Declaration of Competing Interest

The authors declare that they have no known competing financial interests or personal relationships that could have appeared to influence the work reported in this paper.

Acknowledgments:

This work was supported by grants from the National Natural Science Foundation of China (41921001), the China Postdoctoral Science Foundation (2021M693444), and the Technology Innovation Center for Land Engineering and Human Settlements, Shaanxi Land Engineering Construction Group Co.,Ltd and Xi'an Jiaotong University (2021WHZ0072). The authors are grateful to the United States Geological Survey (USGS), the European Centre for Medium-Range Weather Forecasts (ECMWF), and Google Cloud Platform (GCP) for providing Landsat OLI images, water vapor content, and the computation resources.

Appendix A. Supplementary material

Supplementary data to this article can be found online at https://doi.org/10.1016/j.isprsjprs.2021.12.003.

References

AIRBUS. Global Market Forecast. Available online: https://www.airbus.com/content/dam/corporate-topics/financial-and-company-information/Global-Market-Forecast-presentation-Andrew-Gordon-Redburn.pdf. (Accessed 21/05/2021).

Bock, L., Burkhardt, U., 2016. Reassessing properties and radiative forcing of contrail cirrus using a climate model. J. Geophys. Res. Atmos. 121 (16), 9717–9736.

Burkhardt, U., Kärcher, B., 2011. Global radiative forcing from contrail cirrus. Nat. Clim. Chang. 1 (1), 54–58.

Costin, A., Francillon, A., 2012. Ghost in the Air (Traffic): On insecurity of ADS-B protocol and practical attacks on ADS-B devices. In: Black Hat. Las Vegas, LV USA, pp. 1–12.

Chen, C.C., Gettelman, A., 2013. Simulated radiative forcing from contrails and contrail cirrus. Atmos. Chem. Phys. 13 (24), 12525–12536.

Elamaran, V., Balaji, V.S., Kumar, S.R., Upadhyay, H.N., 2018. Single event upset mitatigation techniques on land remote sensing images. Int. J. Pure. Appl. Math. 119 (7), 2633–2643.

Frey, R.A., Ackerman, S.A., Liu, Y., Strabala, K.I., Zhang, H., Key, J.R., Wang, X., 2008. Cloud Detection with MODIS. Part I: Improvements in the MODIS Cloud Mask for Collection 5. J. Atmos. Ocean. Technol. 25 (7), 1057–1072.

Finlay, C.C., Kloss, C., Olsen, N., Hammer, M.D., Tøffner-Clausen, L., Grayver, A., Kuvshinov, A., 2020. The CHAOS-7 geomagnetic field model and observed changes in the South Atlantic Anomaly. Earth, Planets Space. 72 (1), 1–31.

Gorelick, N., Hancher, M., Dixon, M., Ilyushchenko, S., Thau, D., Moore, R., 2017. Google Earth Engine: Planetary-scale geospatial analysis for everyone. Remote Sens. Environ. 202, 18–27.

Gao, B.C., Kaufman, Y.J., 1995. Selection of the 1.375-μm MODIS channel for remote sensing of cirrus clouds and stratospheric aerosols from space. J. Atmos. Sci. 52 (23), 4231–4237.

Heiselberg, H., 2019. Aircraft and Ship Velocity Determination in Sentinel-2 Multispectral Images. Sensors 19 (13), 2873.

Heiselberg, P., Heiselberg, H., 2021. Aircraft Detection above Clouds by Sentinel-2 MSI Parallax. Remote Sens. 13 (15), 3016.

Hersbach, H., Bell, B., Berrisford, P., Hirahara, S., Horányi, A., Muñoz-Sabater, J., Nicolas, J., Peubey, C., Radu, R., Schepers, D., Simmons, A., Soci, C., Abdalla, S., Abellan, X., Balsamo, G., Bechtold, P., Biavati, G., Bidlot, J., Bonavita, M., Chiara, G., Dahlgren, P., Dee, D., Diamantakis, M., Dragani, R., Flemming, J., Forbes, R., Fuentes, M., Geer, A., Haimberger, L., Healy, S., Hogan, R.J., Hólm, E., Janisková, M., Keeley, S., Laloyaux, P., Lopez, P., Lupu, C., Radnoti, G., Rosnay, P., Rozum, I., Vamborg, F., Villaume, S., Thépaut, J.-N., 2020. The ERA5 global reanalysis. Q. J. R. Meteorol. Soc. 146 (730), 1999–2049.

Lee, D.S., Fahey, D.W., Skowron, A., Allen, M.R., Burkhardt, U., Chen, Q., Doherty, S.J., Freeman, S., Forster, P.M., Fuglestvedt, J., Gettelman, A., De León, R.R., Lim, L.L., Lund, M.T., Millar, R.J., Owen, B., Penner, J.E., Pitari, G., Prather, M.J., Sausen, R., Wilcox, L.J., 2021. The contribution of global aviation to anthropogenic climate forcing for 2000 to 2018. Atmos. Environ. 244, 117834.

Liu, G., Sun, X., Fu, K., Wang, H., 2013. Aircraft recognition in high-resolution satellite images using coarse-to-fine shape prior. IEEE Geosci. Remote Sens. Lett. 10 (3), 573–577.

Liu, Y., Hu, C., Zhan, W., Sun, C., Murch, B., Ma, L., 2018. Identifying industrial heat sources using time-series of the VIIRS Nightfire product with an object-oriented approach. Remote Sens. Environ. 204, 347–365.

Liu, Y., Xu, B., Zhi, W., Hu, C., Dong, Y., Jin, S., Lu, Y., Chen, T., Xu, W., Liu, Y., Zhao, B., Lu, W., 2020. Space eye on flying aircraft: From Sentinel-2 MSI parallax to hybrid computing. Remote Sens. Environ. 246, 111867. https://doi.org/10.1016/j.rse.2020.111867.

Le Quéré, C., Jackson, R.B., Jones, M.W., Smith, A.J.P., Abernethy, S., Andrew, R.M., De-Gol, A.J., Willis, D.R., Shan, Y., Canadell, J.G., Friedlingstein, P., Creutzig, F., Peters, G.P., 2020. Temporary reduction in daily global CO_2 emissions during the COVID-19 forced confinement. Nat. Clim. Chang. 10 (7), 647–653.

Irons, J.R., Dwyer, J.L., Barsi, J.A., 2012. The next Landsat satellite: The Landsat data continuity mission. Remote Sens. Environ. 122, 11–21.

International Civil Aviation Organization. Effects of Novel Coronavirus (COVID-19) on Civil Aviation: Economic Impact Analysis. Available online: https://www.icao.int/sustainability/Documents/COVID-19/ICAO%20COVID%202020%2011%2024%20Economic%20Impact.pdf. (Accessed 24/11/2020).

Kärcher, B., 2018. Formation and radiative forcing of contrail cirrus. Nat. Commun. 9, 1824.

Masek, J.G., Wulder, M.A., Markham, B., McCorkel, J., Crawford, C.J., Storey, J., Jenstrom, D.T., 2020. Landsat 9: Empowering open science and applications through continuity. Remote Sens. Environ. 248, 111968. https://doi.org/10.1016/j.rse.2020.111968.

Murray, N.J., Phinn, S.R., DeWitt, M., Ferrari, R., Johnston, R., Lyons, M.B., Clinton, N., Thau, D., Fuller, R.A., 2019. The global distribution and trajectory of tidal flats. Nature 565 (7738), 222–225.

Minnis, P., Schumann, U., Doelling, D.R., Gierens, K.M., Fahey, D.W., 1999. Global distribution of contrail radiative forcing. Geophys. Res. Lett. 26 (13), 1853–1856.

Penner, J.E., 1999. Aviation and the global atmosphere: a special report of the Intergovernmental Panel on Climate Change. Cambridge University Press.

Sausen, R., Isaksen, I., Grewe, V., Hauglustaine, D., Lee, D.S., Myhre, G., Köhler, M.O., Pitari, G., Schumann, U., Stordal, F., Zerefos, C., 2005. Aviation radiative forcing in 2000: An update on IPCC (1999). Meteorol. Z. 14 (4), 555–561.

Schumann, U., 2012. A contrail cirrus prediction model. Geosci. Model Dev. 5 (3), 543–580.

Skowron, A., Lee, D.S., De León, R.R., Lim, L.L., Owen, B., 2021. Greater fuel efficiency is potentially preferable to reducing NOx emissions for aviation's climate impacts. Nat. Commun. 12 (1), 1–8.

Schumann, U., Bugliaro, L., Dörnbrack, A., Baumann, R., Voigt, C., 2021. Aviation contrail cirrus and radiative forcing over Europe during 6 months of COVID-19. Geophys. Res. Lett. 48 (8).

Shi, L., Tang, Z., Wang, T., Xu, X., Liu, J., Zhang, J., 2021. Aircraft detection in remote sensing images based on deconvolution and position attention. Int. J. Remote Sens. 42 (11), 4241–4260.

Tamiminia, H., Salehi, B., Mahdianpari, M., Quackenbush, L., Adeli, S., Brisco, B., 2020. Google Earth Engine for geo-big data applications: A meta-analysis and systematic review. ISPRS-J. Photogramm. Remote Sens. 164, 152–170.

Wei, H., Zhang, Y., Wang, B., Yang, Y., Li, H., Wang, H., 2021. X-LineNet: Detecting aircraft in remote sensing images by a pair of intersecting line segments. IEEE Trans. Geosci. Remote Sens. 59 (2), 1645–1659.

Wu, Q., Sun, H., Sun, X., Zhang, D., Fu, K., Wang, H., 2015. Aircraft Recognition in High-Resolution Optical Satellite Remote Sensing Images. IEEE Geosci. Remote Sens. Lett. 12 (1), 112–116.

Wu, Z.Z., Wan, S.H., Wang, X.F., Tan, M., Zou, L., Li, X.L., Chen, Y., 2020. A benchmark data set for aircraft type recognition from remote sensing images. Appl. Soft Computing 89, 106132. https://doi.org/10.1016/j.asoc.2020.106132.

Xia, L., Zhao, F., Ma, Y., Sun, Z.W., Shen, X.Y., Mao, K.B., 2015. An Improved Algorithm for the Detection of Cirrus Clouds in the Tibetan Plateau Using VIIRS and MODIS Data. J. Atmos. Ocean. Technol. 32 (11), 2125–2129.

Xia, L., Zhao, F., Chen, L., Zhang, R., Mao, K., Kylling, A., Ma, Y., 2018. Performance comparison of the MODIS and the VIIRS 1.38 μm cirrus cloud channels using libRadtran and CALIOP data. Remote Sens. Environ. 206, 363–374.

Zhang, L., Zhang, Y., 2017. Airport detection and aircraft recognition based on two-layer saliency model in high spatial resolution remote-sensing images. IEEE J. Sel. Top. Appl. Earth Obs. Remote Sens. 10 (4), 1511–1524.

Zhao, F., Xia, L., Kylling, A., Li, R.Q., Shang, H., Xu, M., 2018. Detection flying aircraft from Landsat 8 OLI data. ISPRS-J. Photogramm. Remote Sens. 141, 176–184.